J. Fluid Mech. (2003), *vol.* 481, *pp.* 187–213.
DOI: 10.1017/S0022112003003835 Printed in the United Kingdom

Chaotic flows in pulsating cylindrical tubes: a class of exact Navier–Stokes solutions

By MARK G. BLYTH[1]†, PHILIP HALL[1] AND DEMETRIOS T. PAPAGEORGIOU[2]

[1]Department of Mathematics, Imperial College of Science, Technology and Medicine, London SW7 2BZ, UK

[2]Department of Mathematical Sciences, and Center for Applied Mathematics and Statistics, New Jersey Institute of Technology, Newark, NJ 07102, USA

(Received 11 March 2002 and in revised form 24 September 2002)

We consider the unsteady motion of a viscous incompressible fluid inside a cylindrical tube whose radius is changing in a prescribed manner. We construct a class of exact solutions of the Navier–Stokes equations in the case when the vessel radius is a function of time alone so that the cross-section is circular and uniform along the pipe axis. The Navier–Stokes equations admit solutions which are governed by nonlinear partial differential equations depending on the radial coordinate and time alone, and forced by the wall motion. These solutions correspond to a wide class of bounded radial stagnation-point flows and are of practical importance. In dimensionless terms, the flow is characterized by two parameters: Δ, the amplitude of the oscillation, and R, the Reynolds number for the flow. We study flows driven by a time-periodic wall motion, and find that at small R the flow is synchronous with the forcing and as R increases a Hopf bifurcation takes place. Subsequent dynamics, as R increases, depend on the value of Δ. For small Δ the Hopf bifurcation leads to quasi-periodic solutions in time, with no further bifurcations occurring – this is supported by an asymptotic high-Reynolds-number boundary layer theory. At intermediate Δ, the Hopf bifurcation is either quasi-periodic (for the smaller Δ) or subharmonic (for larger Δ), and the solutions tend to a chaotic attractor at sufficiently large R; the route to chaos is found not to follow a Feigenbaum scenario. At larger values of Δ, we find that the solution remains time periodic as R increases, with solution branches supporting periods of successive integer multiples of the driving period emerging. On a given branch the flow exhibits a self-similarity in both time and space and these features are elucidated by careful numerics and an asymptotic analysis. In contrast to the two-dimensional case (see Hall & Papageorgiou 1999) chaos is not found at either small or comparatively large Δ.

1. Introduction

Viscous flow in a circular tube driven by oscillatory wall motion has numerous practical applications, including blood flow, piezo-driven drop-on-demand ink jet printing and mixing processes. A recent physiological application is transmyocardial laser revascularisation (TMLR), which was partly modelled and analysed by Waters (2001). This novel medical procedure involves the laser drilling of narrow circular

† Present address: School of Mathematics, University of East Anglia, Norwich NR4 7TJ, UK.

tunnels through the heart muscle as a way of feeding oxygenated blood to regions that are not sufficiently supplied by the coronary circulation (see Waters 2001 for details as well as the medical article by Horvath *et al.* 1995 and references therein). The tunnels are filled with oxygenated blood and the heart beating causes a complicated oscillatory flow. The success of the medical procedure hinges on the efficacy of oxygen transport by the flow. Thus, it would be important to understand the underlying flow field.

The present study parallels that of Hall & Papageorgiou (1999) (referred to as HP in what follows) who investigated the incompressible two-dimensional flow in a pulsating channel. Solutions can be constructed which are of stagnation-point form, leading to a class of exact Navier–Stokes solutions involving time and the vertical coordinate alone. (This type of flow is used in the study of Waters 2001.) We briefly describe the results of HP in order to emphasize the differences between that and the present study. The relevant bifurcation parameters for these problems are the wall oscillation amplitude Δ and the Reynolds number R based on the frequency of oscillation. Using numerical experiments, HP find that the flow loses vertical symmetry through a symmetry-breaking bifurcation at some R and for all values of Δ. Eventually the flow becomes chaotic as R increases, the route to chaos depending on the value of Δ. At small Δ, a Hopf bifurcation takes place making the flow quasi-periodic in time with a relatively small second frequency (the driving frequency in HP is 2). As R is increased further, a period doubling on the second frequency takes place and the quasi-periodic flow tends to a chaotic attractor at a finite value of R. This route was also analysed using a multiple-scales boundary layer theory that predicts the period doubling on the second frequency and verifies the numerical observations. At relatively large values of Δ the flow becomes chaotic after a period-doubling cascade based on the primary driving frequency – the route to chaos was shown to follow the Feigenbaum scenario and the first universal Feigenbaum constant was calculated numerically with excellent agreement (see Feigenbaum 1979, 1980). At intermediate values of Δ, the solution retains features from both the smaller- and larger-Δ results discussed above. Eventually, however, sufficiently large Reynolds numbers lead to chaotic flow from a Feigenbaum cascade or a quasi-periodic flow.

Pulsating axisymmetric flow is here examined in an infinitely long cylindrical pipe whose wall moves periodically in time. Some aspects of this problem were studied by Secomb (1978) who considered the limits of high- or low-frequency oscillations of small amplitude – there is therefore little overlap between his paper and the present study. The main objective of this work is to compute solutions over a wide range of parameter values where asymptotic theories are not applicable. We achieve this by implementing numerical techniques which are highly accurate and suitable for computing evolving high-Reynolds-number flows. This is managed by use of the streamfunction–vorticity formulation of the Navier–Stokes equations in axisymmetric geometries, second-order finite differences in space, and a fourth-order Runge–Kutta integration in time (for implementations of this method to the two-dimensional Navier–Stokes equations see E & Liu 1996).

The results fall into the three categories of small, intermediate and relatively large Δ (note that in our formulation $\Delta < 1$). With the exception of intermediate values of Δ, the results differ significantly from the two-dimensional case of HP. (In passing, it is worth highlighting that the axisymmetric problem cannot undergo the symmetry-breaking bifurcations that are ubiquitous in the pulsating channel problem.) For small values of Δ, the flow is synchronous with the forcing up to a critical value of R, where a Hopf bifurcation leading to quasi-periodic behaviour occurs. Unlike the channel problem (see HP), this solution is found not to bifurcate again and quasi-periodic behaviour with two frequencies persists (at least for all values of R computed – as high

1.5×10^4). Even though this conclusion is quite difficult to establish fully numerically due to the large values of R that are required, we provide very strong corroborating evidence for the absence of chaos at small Δ by carrying out a boundary layer analysis valid at large R and small Δ with $\Delta \sim R^{-1/2}$ (this scaling is guided by the full calculations and denotes a curve in the (Δ, R)-plane where the Hopf bifurcation enters). The result of the boundary layer analysis is a steady-streaming problem which evolves on timescales dictated by the second frequency which decreases as $1/R$ with increasing R (this observation again comes from the simulations). Numerical solutions of the steady-streaming problem yield-time-periodic flows at streaming Reynolds numbers as high as 5×10^3. This axisymmetric steady-streaming problem is the same as the accelerating wall exact Navier–Stokes problem of Brady & Acrivos (1981), when the walls move inwards towards the origin.

When Δ is relatively large ($\geqslant 0.45$), the flow is found to be time periodic. In §4.2 we consider in detail the typical case $\Delta = 0.6$. The behaviour as R increases is as follows: At values of R up to about 590 the flow is synchronous with the forcing, which has period π in our case. This branch of solutions loses stability at approximately this value and a disjoint branch of 2π-periodic solutions becomes more attracting. As R is increased further, the 2π-branch loses stability to a disjoint 3π-branch. This pattern appears to continue indefinitely, with a $n\pi$-branch being replaced with a $(n+1)\pi$-branch at a critical value of R. The solutions on a given branch have multiple timescales which essentially are $n\pi$, π and a shorter adjustment timescale that takes the flow from one period to the next. The solutions in each branch, and in particular those supported at high Reynolds numbers, exhibit some intricate self-similar structures both in time and space.

The layout of the paper is as follows. In §3 we formulate the problem and give the governing equations in vorticity–streamfunction form. In §4 we describe in detail our numerical methods and diagnostic data processing techniques. In §5 we present our results. Section 6 is devoted to the small-Δ large-R steady streaming problem and §7 contains our conclusions.

2. Statement of the problem

We consider the flow of an incompressible fluid in an infinitely long straight circular pipe with a rigid wall, whose radius is allowed to vary in time in a prescribed periodic manner. We adopt cylindrical polar coordinates (r, θ, z) and assume the flow to be axisymmetric. In this case, we may introduce a time-dependent streamfunction $\psi(r, z, t)$, defined by

$$u = -\frac{1}{r}\frac{\partial \psi}{\partial z}, \quad w = \frac{1}{r}\frac{\partial \psi}{\partial r}. \tag{2.1}$$

We also define the vorticity $\omega = \nabla \times \boldsymbol{u} = \Omega(r, z, t)e_\theta$, where $\boldsymbol{u} = u(r, z, t)e_r + \omega(r, z, t)e_z$. If the fluid in question has kinematic viscosity ν, and is to undergo a squeezing motion of typical frequency n with mean radius $\overline{a}$, we non-dimensionalize by writing $t^* = nt$, $(r, z) = (\overline{a}r^*, \overline{a}z^*)$, and $\psi = n\overline{a}^3\psi^*$, $\Omega = n\Omega^*$. The pipe radius $a(t) = \overline{a}H^*(t)$. Asterisks denote dimensionless variables. These will be dropped forthwith for convenience. The Navier–Stokes equations may then be written in streamfunction–vorticity form as

$$\Omega_t - \psi_z\left(\frac{\Omega}{r}\right)_r + \frac{1}{r}\psi_r\Omega_z = \frac{1}{R}\left[\Omega_{rr} + \left(\frac{\Omega}{r}\right)_r + \Omega_{zz}\right], \tag{2.2a}$$

$$\psi_{rr} - \frac{1}{r}\psi_r + \psi_{zz} = -r\Omega, \tag{2.2b}$$

where $R = n\bar{a}^2/\nu$ is the Reynolds number of the flow. The boundary conditions are those of no-slip at the wall and regularity at the origin. These will be given explicitly below.

Solutions of stagnation-point form exist for this flow, and these can be written as

$$\psi = zrF(r,t), \quad \Omega = zG(r,t). \tag{2.3}$$

These provide exact solutions of the Navier–Stokes equations in the sense that a system of PDEs, depending on one space coordinate and time, follows from the full equations without approximation.

Using the forms (2.3) and fixing the flow domain by the transformation $\eta = r/H(t)$, the Navier–Stokes equations (2.2) become

$$G_t - \frac{\dot{H}}{H}\eta G_\eta - \frac{1}{H}FG_\eta + \frac{1}{H}F_\eta G + \frac{2FG}{\eta H} = \frac{1}{H^2R}\left[G_{\eta\eta} + \frac{1}{\eta}G_\eta - \frac{G}{\eta^2}\right], \tag{2.4a}$$

$$F_{\eta\eta} + \frac{1}{\eta}F_\eta - \frac{1}{\eta^2}F = -H^2G, \tag{2.4b}$$

with boundary conditions

$$F(0,t) = 0, \quad G(0,t) = 0, \tag{2.5a}$$

$$F(1,t) = -\dot{H}, \quad F_\eta(1,t) = \dot{H}. \tag{2.5b}$$

The axisymmetry of the flow means that u and w_η are zero at the origin, implying $F(0,t) = 0$ and $G(0,t) = 0$, respectively. As mentioned above, the wall motion is prescribed in advance, and in particular we take

$$H(t) = 1 + \Delta\cos(2t), \quad 0 < \Delta < 1. \tag{2.6}$$

The parameter Δ represents the oscillation amplitude. Note that without loss of generality we choose the frequency of the wall forcing to be 2. Different frequencies may be accounted for by varying the size of the Reynolds number. This is evident through the non-dimensionalization above.

The system (2.4), together with (2.5), defines the problem to be studied throughout the rest of this paper for different values of R, Δ. In the limit of zero Reynolds number the viscous terms dominate and a unique, stable quasi-static Poiseuille flow is found which is synchronous with the wall motion. Denoting this periodic solution with the subscript B, we find for $R \ll 1$,

$$F_B = \dot{H}\eta(\eta^2 - 2) + O(R), \tag{2.7a}$$

$$G_B = -8\eta\dot{H}/H^2 + O(R). \tag{2.7b}$$

Similar small-Reynolds-number results are found in the channel problem (see HP and Stuart *et al.* 1990); a central difference between the channel and pipe geometries is that the former can undergo symmetry-breaking bifurcations about the centre, something that is not possible in axisymmetric geometries. As shown in HP, the flows which are initially symmetric at small Reynolds numbers undergo symmetry-breaking bifurcations which then lead to temporal Hopf bifurcations at lower Reynolds numbers than those found if symmetry is forced. The Hopf bifurcations lead to chaotic behaviour as discussed in HP. In the axisymmetric problem, temporal chaotic or quasi-periodic structures are found to emerge at larger Reynolds numbers, as would be expected.

In general, then, for higher Reynolds numbers numerical techniques must be employed in order to construct quantitative features of the solutions and to build

a bifurcation picture of the most attracting dynamics. This is pursued in the next section.

3. Numerical methods

In this section we describe the numerical method used to solve (2.4), (2.5), and the diagnostic tools used to interpret the dynamics. The numerical procedure is based on a fourth-order Runge–Kutta integration in time with second-order central differences in space. It is a modified version of a method developed for the Navier–Stokes equations by E & Liu (1996), which is suitable for high Reynolds numbers. We first rewrite equations (2.4) as

$$\mathrm{L}F = -H^2 G \qquad \left(\mathrm{L} \equiv \frac{\partial^2}{\partial \eta^2} + \frac{1}{\eta}\frac{\partial}{\partial \eta} - \frac{1}{\eta^2}\right), \tag{3.1}$$

$$G_t = M(t, F, G; R), \tag{3.2}$$

with M containing all linear and nonlinear terms of (2.4*a*). The method is a four-stage one and is given below. We use the notation $F^n(\eta) = F(\eta, t_n)$ etc., to obtain

$$\frac{G_1 - G^n}{(\Delta t/2)} = M(t_n, F^n, G^n) \qquad F_1 = \mathrm{L}^{-1}\left(-H^2\left(t_n + \tfrac{1}{2}\Delta t\right)G_1\right), \tag{3.3}$$

$$\frac{G_2 - G^n}{(\Delta t/2)} = M\left(t_n + \tfrac{1}{2}\Delta t, F_1, G_1\right) \qquad F_2 = \mathrm{L}^{-1}\left(-H^2\left(t_n + \tfrac{1}{2}\Delta t\right)G_2\right), \tag{3.4}$$

$$\frac{G_3 - G^n}{\Delta t} = M\left(t_n + \tfrac{1}{2}\Delta t, F_2, G_2\right) \qquad F_3 = \mathrm{L}^{-1}\left(-H^2(t_n + \Delta t)G_3\right), \tag{3.5}$$

$$k_4 = \Delta t\, M(t_n + \Delta t, F_3, G_3), \tag{3.6}$$

and the solution at level t_{n+1} is given by

$$G^{n+1} = \tfrac{1}{3}(-G^n + G_1 + 2G_2 + G_3) + \tfrac{1}{6}k_4, \tag{3.7}$$

$$F^{n+1} = \mathrm{L}^{-1}(-H^2(t_n + \Delta t)G^{n+1}). \tag{3.8}$$

In the expressions above, the inverse operator L^{-1} is performed numerically and typically involves a single tridiagonal solve. Each timestep involves four tridiagonal solvers and the method is very efficient as well as accurate. We note that for the Navier–Stokes problem, the operator L is the Laplace operator and the cost increases accordingly.

The discretization in η is performed on a regularly spaced grid $\eta_i = (i-1)\Delta\eta$ for $i = 1, \ldots, N$, with the points $\eta_1 = 0$ and $\eta_N = 1$ corresponding to the pipe axis and wall respectively. The discrete values of the functions G_1, G_2 and G_3 are obtained in a straightforward way at the interior points $\eta_2, \ldots, \eta_{N-1}$ from the first of each of equations (3.3)–(3.5). Their values at η_1 and η_N are not required to obtain the discrete values of F_1, F_2, F_3 from the tridiagonal inversion since boundary conditions for F are known at η_1 and η_N (see (2.5)). The same is true for equation (3.8) at level t_{n+1}. There are two boundary conditions for F available at $\eta = 1$ as seen from (2.5*b*). In solving the tridiagonal systems in (3.3)–(3.8), we use the Dirichlet condition $F(1, t) = -\dot{H}$. The other condition is used at the end of the step, that is after (3.7) is solved at $\eta_2, \ldots, \eta_{N-1}$ and (3.8) is solved at $\eta_1, \ldots, \eta_N$, in order to obtain the boundary values of G^{n+1}. The condition at η_1 follows from (2.5*a*) as $G_1^{n+1} = 0$. At η_N we use the definition of vorticity (3.1). If we introduce a fictitious point outside the

domain at η_{N+1}, then we can apply central differences to the condition $F_\eta = \dot{H}$ at η_N (see (2.5a)) to obtain

$$F^k_{N+1} = F^k_{N-1} + 2\Delta\eta\dot{H}(t_k).$$

A central difference of (3.1), then, and elimination of the fictitious point values gives the following boundary conditions for G to be applied at the end of the kth timestep:

$$G^k_1 = 0, \qquad G^k_N = -\frac{2}{H^2(t_k)}\left[\frac{F^k_{N-1} - F^k_N + h\dot{H}(t_k)}{h^2} + \dot{H}(t_k)\right]. \tag{3.9}$$

This completes the numerical method. Stability is discussed in E & Liu (1996) and we note that the method has good stability properties at high R.

3.1. *Diagnostics*

Detailed numerical results have been computed for various values of the Reynolds number, R, and the wall oscillation amplitude, Δ. The diagnostic tools employed to interpret the results are discussed below. Further details can be found in HP (see also Bergé, Pomeau & Vidal 1984 and Eckmann & Ruelle 1985).

We use various means to describe the flow dynamics. A time series is set up by tracking the value of the vorticity at the pipe wall, that is we define $\alpha(t) = G(\eta = 1, t)$. A second diagnostic is constructed by defining a trajectory in three-dimensional space by $\boldsymbol{x}(t) = (x_1(t), x_2(t), x_3(t)) = (G(1/4, t), G(1/2, t), G(3/4, t))$. This trajectory is then used to construct a Poincaré section whenever $x_3(t)$ becomes zero (such points are found by interpolation).

From these definitions the following conclusions are possible. If the flow is synchronous with the forcing, then $\alpha(t)$ is periodic of period π, while period–doublings give periods 2π, 4π and so on. One way to visualize and distinguish between different period flows (or indeed non-periodic and chaotic ones) is to consider the two sets of points (t_i, m_i), (t_j, M_j) for $i, j = 1, 2, \ldots$, where m_i and M_j are the successive minima and maxima of the time series $\alpha(t)$. For example, if the flow is periodic of period π then all $m_i = m_{i+1}$, $M_j = M_{j+1}$ for all sufficiently large i, j (after transients die out), while $t_{i+1} - t_i = \pi$. Visually, all the minima and maxima lie on exactly one straight line respectively in the min/max-t plane. If a period doubling takes place, then the minima and maxima will lie on two distinct straight lines respectively with $t_{i+2} - t_i = 2\pi$ and the picture generalizes to many period doublings. Chaotic or irregular behaviour is manifested by a seemingly unstructured set of minima and maxima. Return maps are constructed by plotting, for example, (m_i, m_{i+1}), $i = 1, 2, \ldots$. These are useful in deciding whether or not the flow is chaotic and exhibits foldings and self-similarity. To complete the picture, we note that periodic flows produce return maps (as defined above) which consist of k points for $k\pi$-periodic flows for integer k. Quasiperiodic solutions emerge as filled lines or sets of such lines when the return map is considered. Similar conclusions can be drawn from the Poincaré sections also.

Lyapunov exponents may be calculated as a further diagnostic of chaos. These are computed by considering the rate of separation of particle paths which are initially very close together. For two particles with position vectors $\boldsymbol{r}_i = (\eta_i, z_i)$, $i = 1, 2$ with initial separation $|\delta\boldsymbol{r}_0| = |\boldsymbol{r}_2 - \boldsymbol{r}_1|$ at $t = t_0$, the Lyapunov exponent is defined to be

$$\lambda = \lim_{t\to\infty} \frac{1}{t - t_0} \ln \frac{|\delta\boldsymbol{r}|}{|\delta\boldsymbol{r}_0|}$$

(e.g. Ottino 1989). For a chaotic flow, λ is expected to be positive. In this case the particle paths rapidly diverge and in the practical computation of the exponent it is periodically necessary to renormalize the distance between the two paths while preserving the orientation of the separation vector $\boldsymbol{\delta r}$ (see, for example, Wolf *et al.* 1985). The exponent is calculated at each renormalization and the average of these values should tend to a constant (the maximum Lyapunov exponent) as t increases. The particle paths are computed using fourth-order Runge–Kutta integration.

4. Solutions as the wall oscillation amplitude increases

As has been indicated in (2.7), at small Reynolds numbers a unique, stable solution in synchrony with the wall forcing exists. One important difference from HP's work which should be noted is that there is no equivalent vertical symmetry here and hence no symmetry-breaking bifurcation is encountered as the Reynolds number is increased from zero. Instead the flow tends to remain synchronous with the wall motion until a Hopf bifurcation introduces a second frequency, which is incommensurate with the forcing frequency, and quasi-periodicity ensues. Since we will solve the governing equations numerically by marching forward in time from an arbitrary initial state as described above, we should lock on to the most stable solution in the vicinity of the initial state. However, as the Reynolds number increases and the dynamics become increasingly rich, there exists the possibility of numerics hopping from one attractor to a near neighbour during the simulation. Various methods are employed to follow a particular attractor dynamically, and these are discussed as they arise in the text.

4.1. *Moderate and relatively small* Δ

4.1.1. *The case* $\Delta = 0.3$

We begin by presenting results for the case $\Delta = 0.3$. The initial conditions for both F and G are taken to be zero for all η.

At low values of R, the flow is synchronous with the forcing leading to time-periodic solutions of period π. A Hopf bifurcation takes place at a value of R between 655.0 and 660.0 with the flow being 2π-periodic. The bifurcation diagram is shown in figure 1, which shows the positions of the maxima of $\alpha(t)$ defined above (after transients have disappeared) as the Reynolds number is increased. All the results in figure 1 were calculated using 600 points in the η-direction and a timestep of 0.0005.

At higher Reynolds numbers still, the situation becomes increasingly complicated. Different attractors compete and our numerical procedure computes the most highly attracting one. For example, starting with zero initial conditions and $R = 860$, the long-time behaviour locks onto a 4π-periodic solution after about 100 time units. Clearly (see figure 1) this attractor co-exists with the 2π-periodic one followed in the figure. We calculated the 2π attractor at $R = 860$ by using as initial conditions the 2π-periodic results for $R = 870$, for example, which was the most attracting solution for zero initial data. Continuation methods can be used to follow different periodic attractors both forward and backwards in R – see HP for such calculations in the case of channel flows.

Given the complicated and mixed behaviour briefly outlined above, we provide sample numerical solutions which bring out the richness of the dynamics involved. We begin with the case $R = 900$. The solution eventually locks onto a 2π-periodic solution after a long transient of chaotic behaviour lasting about 4000 time units. The results are shown in figure 2 where the maxima and minima of $\alpha(t)$ are shown, along

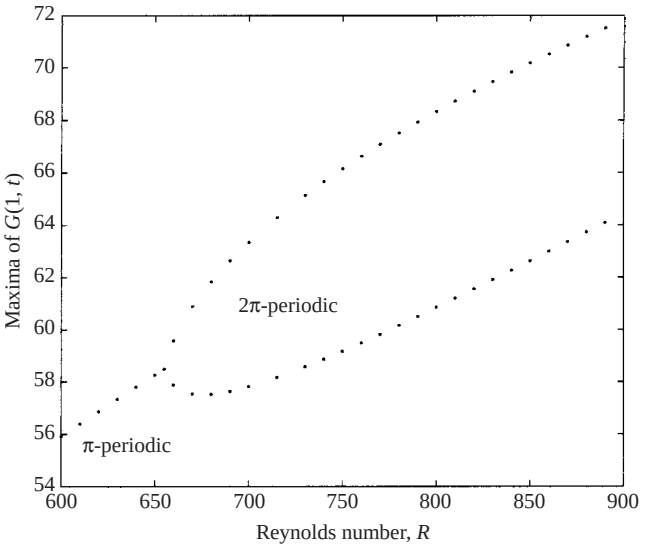

FIGURE 1. Behaviour at moderate values of R for $\Delta = 0.3$.

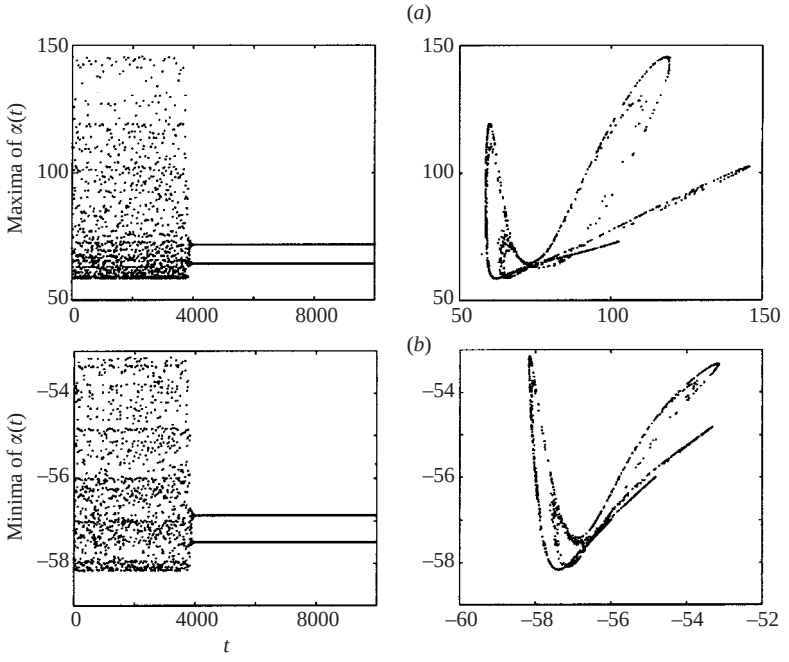

FIGURE 2. The case $R = 900$, $\Delta = 0.3$: (a) maxima and (b) minima of $\alpha(t)$ and their corresponding return maps.

with their corresponding return maps (see above for the construction); the return maps are strong evidence that the transient flow is chaotic.

The case $R = 1000$ is presented next. Here we find persistence of chaotic motion for $t < 8000$. Results are shown in figure 3 (for a description see figure 2). In addition, in figure 4 we show the Poincaré section constructed as described above. Again, foldings

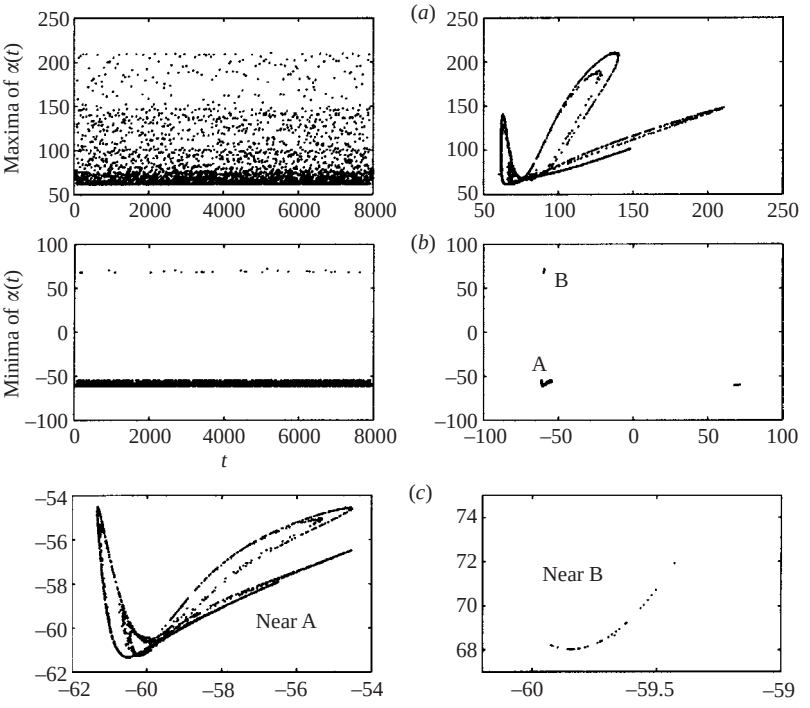

FIGURE 3. The case $R = 1000$, $\Delta = 0.3$. Chaotic solutions: (a) maxima and (b) minima and their corresponding return maps; (c) expanded view near points A and B.

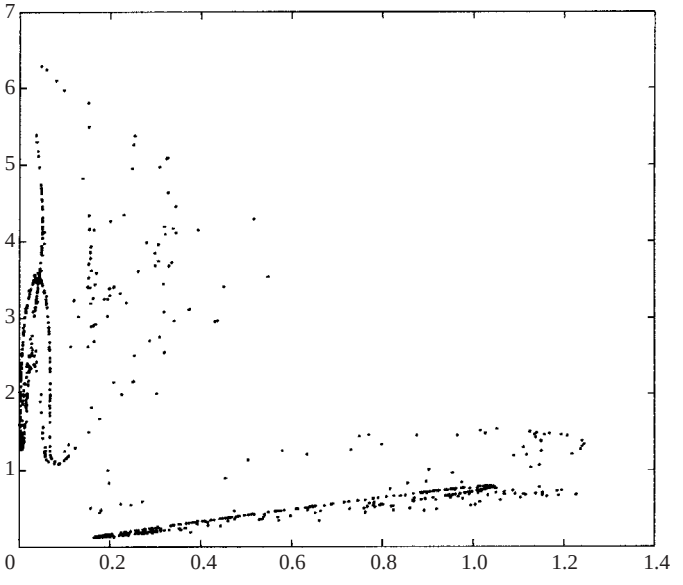

FIGURE 4. The case $R = 1000$, $\Delta = 0.3$. Poincaré section showing chaotic behaviour.

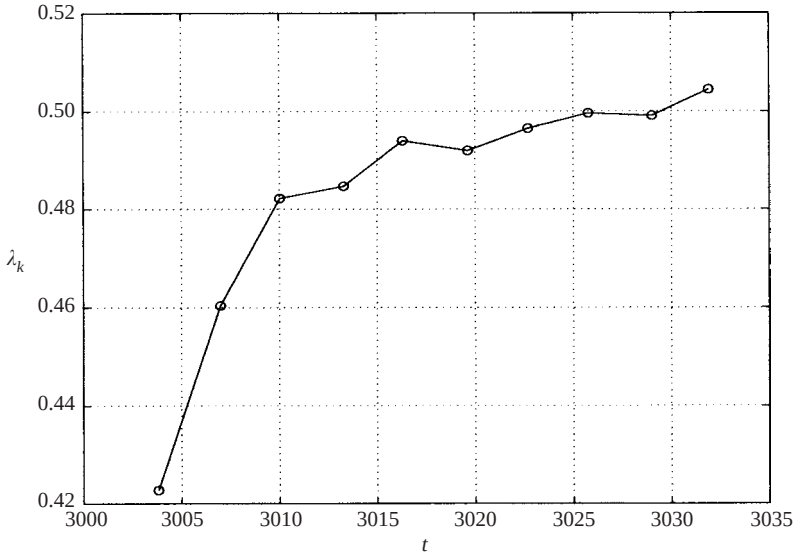

FIGURE 5. Maximum Lyapunov exponent for $\Delta = 0.3$, $R = 1000$. The λ_k are the values of the exponent calculated at each renormalization (see §3).

and self-similarity are present and the existence of a strange attractor can be inferred. In figure 5 we plot the results of the calculation of the maximum Lyapunov exponent, as described in §3. We took $t_0 = 3000$, with $\boldsymbol{r}_1 = 0.6$, $\boldsymbol{\delta r} = 10^{-5}$. The λ_k shown in the figure are those calculated at each renormalization. One difficulty encountered was that particle trajectories tend to rapidly approach either the upper wall or the pipe centreline before which only a few estimates of λ may be obtained. Nevertheless, the fact that the exponent is positive provides further evidence that the dynamics are chaotic.

The case of the minima is particularly interesting since they lie very close together about two mean positions, resulting in return maps which are disjoint, as seen from the enlargements in figure 3(c).

At larger values of R, there coexist time-periodic and chaotic attractors – as emphasized earlier, we are mostly reporting on the large-time dynamics starting from zero initial flow. Results at the relatively large Reynolds numbers of 1500 and 2000 are given in figures 6 and 7, which show the evolution of the maxima of the wall vorticity as time increases. The solution for $R = 1500$ is time-periodic with period 13π (there are thirteen lines in figure 6 corresponding to the values of the maxima of $\alpha(t)$) and for $R = 2000$, after a short transient, the solution is attracted to a 19π-periodic solution (there are 19 horizontal lines in the plot). In figure 8, we include results at the intermediate values $R = 1600, 1700, 1800, 1900$. The plots show the maxima of the time signal $F(1/2, t)$ against the corresponding minima; they provide strong evidence that a chaotic attractor is present, which is the same one for all four values of R. All plots have about 3800 points and are the result of calculations to 10 000 time units – the length of the computation is evidence that the attractors are long-lived (it is impossible to preclude the possibility that they may be a transient, however). It can be concluded, therefore, that chaotic and time-periodic attractors coexist. Chaotic behaviour is typical of intermediate values of Δ, while time-periodic solutions with periods which are increasing (with Reynolds number) integer multiples

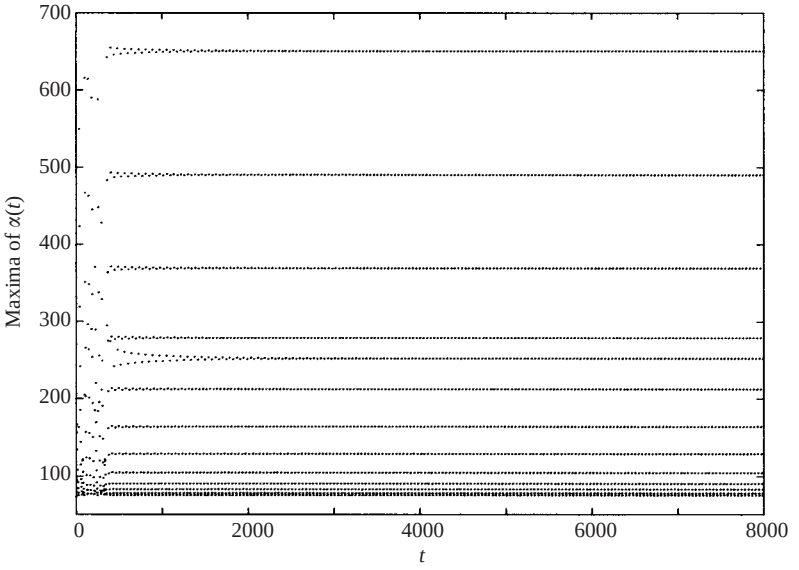

FIGURE 6. The case $R = 1500$, $\Delta = 0.3$. Periodic solutions of period 13π.

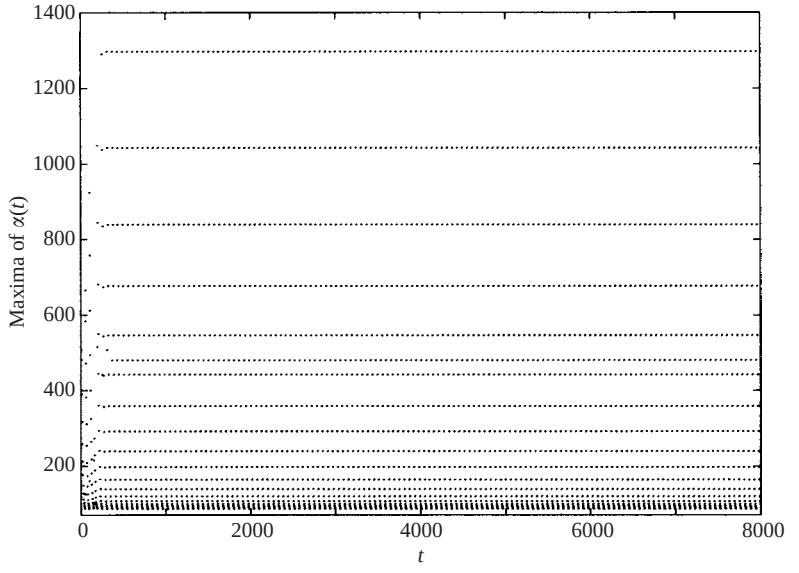

FIGURE 7. The case $R = 2000$, $\Delta = 0.3$. Periodic solutions of period 19π.

of π, the driving period, are a feature of relatively large values of Δ (larger than about 0.5). The latter type of attractor is discussed fully in the following Section.

To illustrate the accuracy of our numerical solutions, we have plotted in figure 9 the maxima of $F(1/2, t)$ for the three cases $N = 601$, $N = 1001$ and $N = 1201$. It is obvious from the picture that convergence is achieved. For the case $R = 1000$, we have verified that increasing the resolution still results in a chaotic solution, with the maxima of $F(1/2, t)$, for example, always lying within the same bounds.

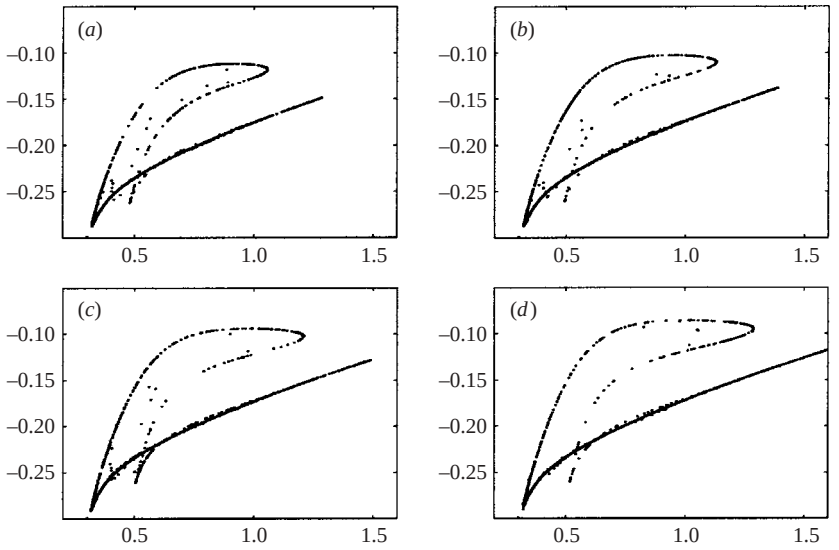

FIGURE 8. $R = (a)\,1600, (b)\,1700, (c)\,1800, (d)\,1900$, all for $\Delta = 0.3$. Chaotic attractors constructed by plotting the maxima of $F(1/2, t)$ against the minima of $F(1/2, t)$.

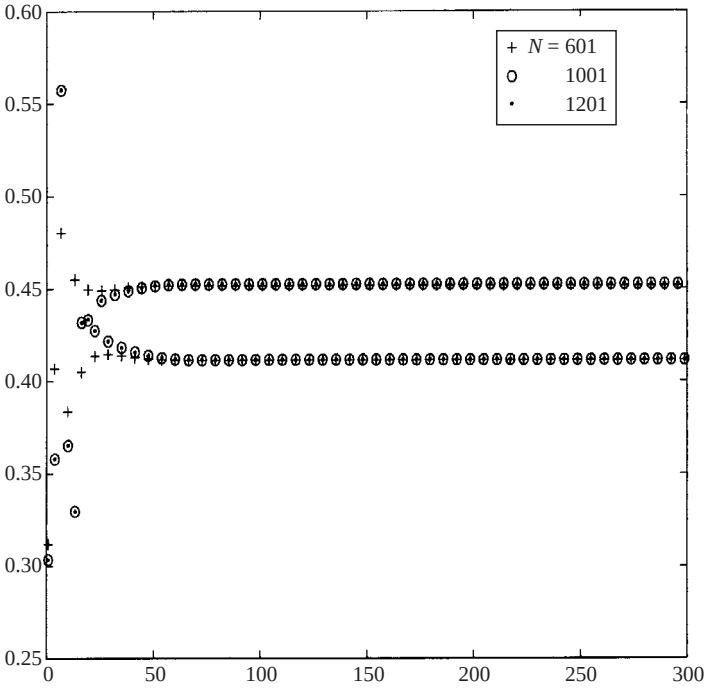

FIGURE 9. $\Delta = 0.3$, $R = 690$: Maxima of $F(1/2, t)$ for various numbers of grid points, N.

4.1.2. *The case* $\Delta = 0.2$

When $\Delta = 0.2$ the results are qualitatively similar to those for $\Delta = 0.3$ except that the flow becomes quasi-periodic in time over a range of Reynolds numbers beyond the initial Hopf bifurcation and before the eventual emergence of chaos as the Reynolds

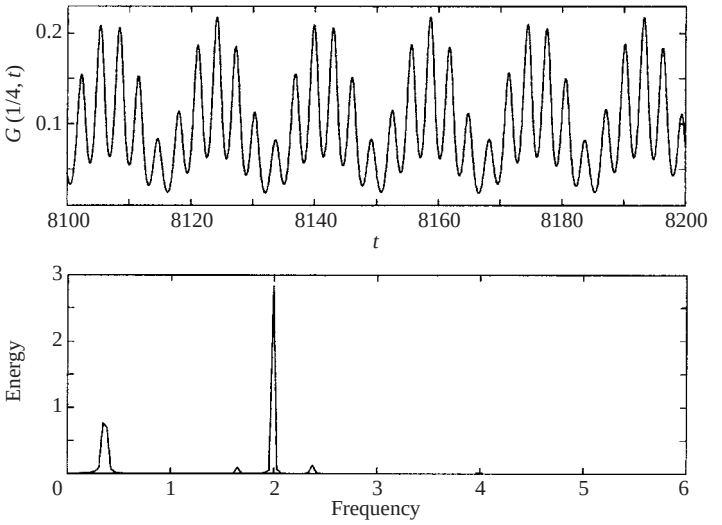

FIGURE 10. Time signal $G(1/4, t)$, and its frequency spectrum for the case $\Delta = 0.2$, $R = 2050$.

number is increased. In this case the flow remains in synchrony with the wall forcing for Reynolds numbers approximately less than 2005. We begin by showing a set of results at $R = 2050$ which is just above the Hopf bifurcation point (about 2.5% above $R = 2005$). Figure 10 shows the time evolution of the scaled vorticity at $\eta = 1/4$, along with the corresponding spectrum. Note that the spectrum is generated from a much longer signal than that depicted, in order to sharply resolve the harmonics–typically 100 periods corresponding to the lower frequency are included. The spectrum shows clearly the driving frequency equal to 2, with the relatively small second frequency resulting from the first Hopf bifurcation. It appears from the time signal that the energy of the bifurcated state is less than that of the driving frequency. The energy spectrum confirms this, showing the ratio between the two to be about a third. This energy partition is slightly different from the channel flow case described in HP, where the Hopf bifurcations contain significantly less energy than the driving frequency (see, for example, figure 7 of HP, for $\Delta = 0.25$, where the energy of the Hopf-bifurcated state is about two orders of magnitude less than that of the driving frequency). The symmetry breaking which is possible in the two-dimensional case, but not the axisymmetric one, allows the solution to keep most of the energy in the wall-synchronous motion. As concluded below, the ratio of the two basic frequencies is irrational and the flow is quasi-periodic in time. Theoretically, a dense spectrum could be seen if the signal becomes increasingly longer – the energy in the other frequencies is very small also, leading to obvious identification difficulties. Strong evidence of the quasi-periodicity is found in constructions of return maps from the maxima or minima of the time signal. Such results are presented in figure 11(*a,b*). The maxima are plotted in figure 11(*a*) over a range of 6000 time units (this scale is responsible for the deceptive joining of points in the figure to produce continuous looking curves). Such a pattern is typical of quasiperiodicity. The accompanying return map in figure 11(*b*) is further strong evidence of a quasi-periodic flow. The loop is dense with points, due to the dominance of two irrational frequencies.

Quasiperiodic solutions were calculated up to and including $R = 2206$ and a periodic solution of period 25π was found at $R = 2212$. We note that the

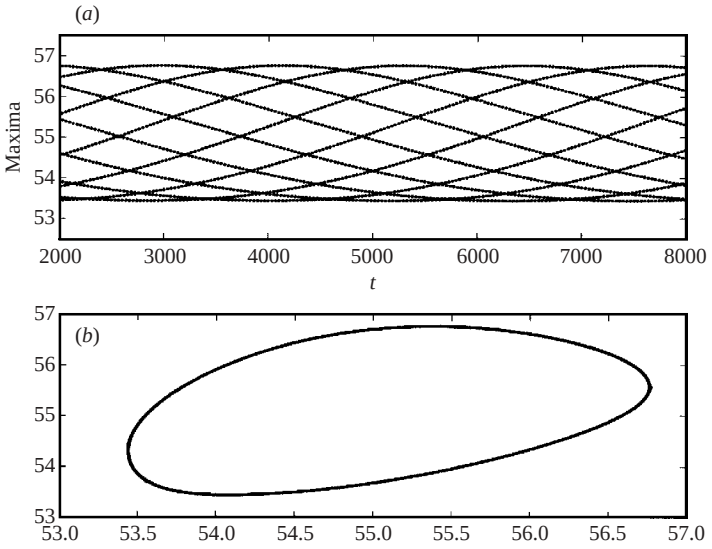

FIGURE 11. The case $\Delta = 0.2$, $R = 2050$. (a) Maxima of $G(1, t)$, (b) the return map of the maxima of $G(1, t)$.

quasi-periodic window between $R = 2005$ and 2212 is not necessarily the only possible attractor; for example, a 6π-periodic solution was found at $R = 2175$, starting from zero initial conditions. Just beyond $R = 2206$ several periodic attractors were found including $(R, \text{period}) = (2212, 25\pi)$, $(2225, 19\pi)$, $(2250, 13\pi)$, $(2300, 7\pi)$, $(2350, 14\pi)$ and $(2400, 7\pi)$. In between these attractors, chaotic solutions were seen at $R = 2270, 2275$. Beyond $R = 2500$, and going as high as $R = 4000$ in increments of 100, all computed solutions were found to be chaotic. Our extensive calculations have not been able to establish a period-doubling route to chaos. This is again in contrast to the two-dimensional case studied in HP, and more discussion on this point is included in the following subsection.

We conclude the case $\Delta = 0.2$ by including two representative chaotic solutions at $R = 2600$ and $R = 4000$ in figure 12(a, b). The return maps of the maxima of $G(1/4, t)$ exhibit noticeable foldings which are highly suggestive of chaos. A calculation of the Lyapunov exponent yields a value of approximately 0.2, which is a further indication that a strange attractor is present.

4.1.3. *The cases* $\Delta < 0.2$

The numerical results for other, smaller, Δ are similar to those described above. The main difference is that the range of Reynolds numbers for which the flow remains quasi-periodic (after the first Hopf bifurcation) increases with decreasing Δ. For example, for $\Delta = 0.15$ the first Hopf bifurcation leading to a two-frequency quasi-periodic solution takes place at approximately $R = 3700$, while the corresponding value for $\Delta = 0.075$ is approximately $R = 15\,700$. Thus the computations require very large values of the Reynolds number, and this leads to difficulties due to the large number of grid points required in order to properly resolve the time-dependent boundary layer at the wall. The dual limit of small wall amplitude and large Reynolds number is crucial, and in what follows we present strong numerical evidence that the relevant scaling to consider as $R \to \infty$ has Δ proportional to $1/R^{1/2}$. The same scaling was also identified as being important for the channel problem discussed in

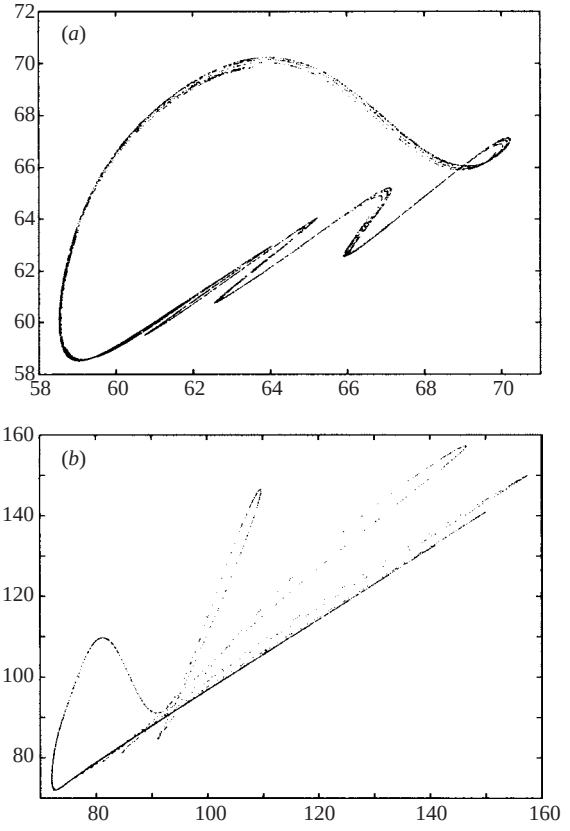

FIGURE 12. Chaotic return maps of maxima for $\Delta = 0.2$, (*a*) $R = 2600$, (*b*) $R = 4000$.

HP. In that paper, a steady streaming boundary layer theory was developed which predicted a period-doubling cascade to chaos on the second, smaller, frequency. This complemented the numerics for the full problem, which also showed such a cascade to chaos. A similar boundary layer theory can be constructed here. We present it later and compare its predictions with the full numerical simulations for small Δ to be described next.

Simulations for the small values $\Delta = 0.2, 0.15, 0.1, 0.075$ were performed at various values of the Reynolds number. For each of these Δ, the critical value of R at which the bifurcation from the base periodic state to quasi-periodic flow takes place is indicated by a circle in figure 13(*a*). The same figure is regraphed in figure 13(*b*) as a log-log plot. The straight line so obtained has a slope of -2, strongly suggesting that the bifurcation occurs when $\Delta \sim R^{-1/2}$.

At the bifurcation a new frequency is introduced into the flow which is much smaller than that due to the wall forcing. Thus two timescales are at play in the new flow: the short timescale of order π associated with the driving mechanism, and a much longer modulational timescale associated with the new frequency. Our numerical results suggest that this longer timescale becomes asymptotically large as the Reynolds number increases; in fact it appears to scale linearly with R. Equivalently, the second frequency tends to zero as the inverse of the Reynolds number. This behaviour is evident in figure 14(*a*), where a time signal is plotted for $\Delta = 0.075$ and $R = 18\,000$ (within the quasi-periodic regime). Note that, as in figure 10(*a*), the modulation

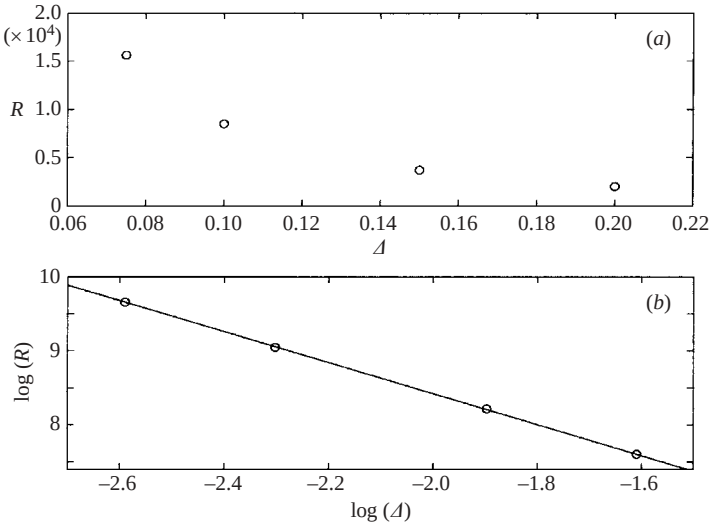

FIGURE 13. The relationship between wall amplitude Δ and Reynolds number R. (a) Data points indicating the onset of quasi-periodicity, (b) a log–log plot of the same data, shown with a line of gradient -2.0.

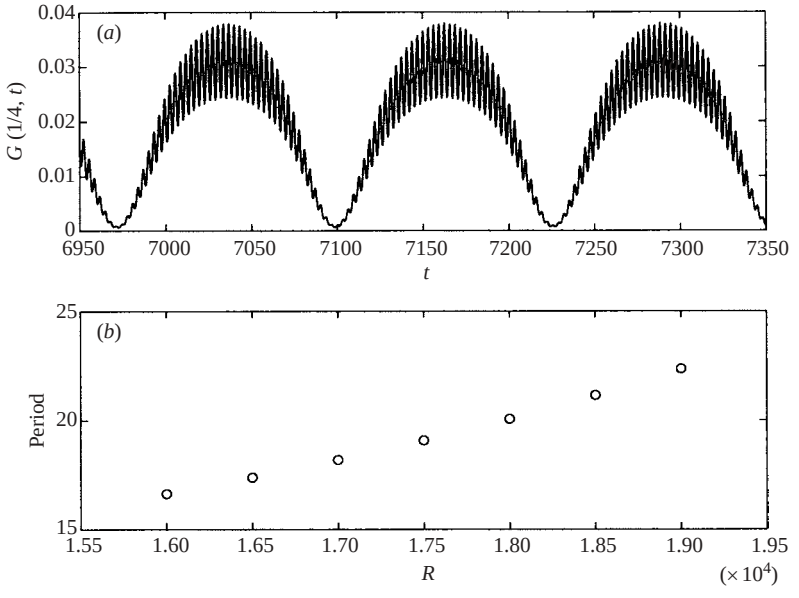

FIGURE 14. The slow variation induced by the second frequency when $\Delta = 0.075$. (a) Time series $G(1/4, t)$ for $R = 18\,000$, (b) dependence of the long modulational periods on Reynolds number.

amplitude is greater than the amplitude of the oscillations on the driving timescale. Calculating the frequency spectrum confirms that the second frequency does indeed have greater energy than the underlying period. As the Reynolds number increases, the second frequency drifts to lower values, without a new Hopf bifurcation being apparent. This conclusion is supported by our asymptotic theory, presented in §5.

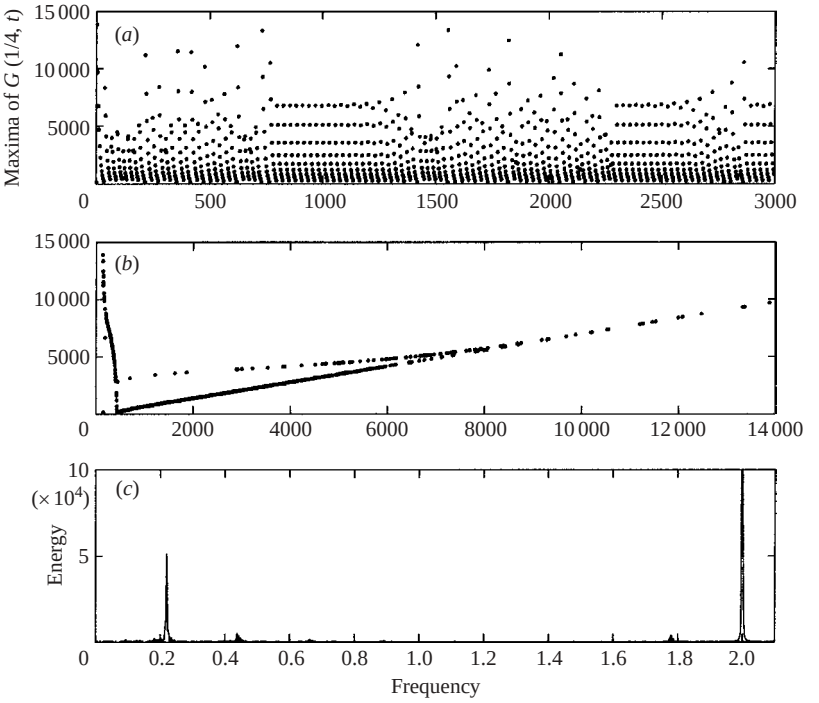

FIGURE 15. Results for $\Delta = 0.45$, $R = 1500$. (*a*) The maxima of $G(1, t)$. (*b*) Return map of the maxima of $G(1, t)$. (*c*) Energy spectrum of the signal $G(1/4, t)$.

As noted above, the modulational period increases (while the second frequency decreases) with Reynolds number, the relationship being approximately linear. This is shown by the data points in figure 14(*b*), where the long quasi-periods associated with the second frequency are plotted against Reynolds number when $\Delta = 0.075$. This result is central to the asymptotic theory.

4.2. *Relatively large amplitude* ($\Delta > 0.45$)

It was found in the previous section that chaotic solutions occur at sufficiently high Reynolds numbers for $\Delta = 0.2$ and $\Delta = 0.3$. In contrast to the channel problem, however, we have not found chaos for values of the wall amplitude larger than 0.45 (the values $\Delta = 0.45, 0.5, 0.6, 0.7$ were considered, and most of the results reported in the latter part of this section are for the typical case $\Delta = 0.6$).

We start with $\Delta = 0.45$. As with previous calculations the flow is π-periodic when the Reynolds number is sufficiently small, and a Hopf bifurcation leading to a 2π-periodic solution occurs at a Reynolds number less than 500. Subsequently, the flow becomes 3π-,4π-periodic at $R = 750$, 900. At higher R the flow alternates between intervals of $n\pi$-periodic solutions (n being an increasing integer as R increases), and what appears to be quasi-periodic behaviour. All integrations were started with zero flow. A typical result is given in figure 15 which shows a plot of the maxima of the wall vorticity when $R = 1500$. The intermittent windows of nine almost straight lines are the result of a co-existing 9π-periodic attractor competing with the quasi-periodic one. Indeed, the energy spectrum plotted in figure 15 shows a peak at a frequency of 0.2205, a slight shift from the value of 2/9 required for the flow to be 9π-periodic. Other calculations exhibit similar intermittency patterns; for example at

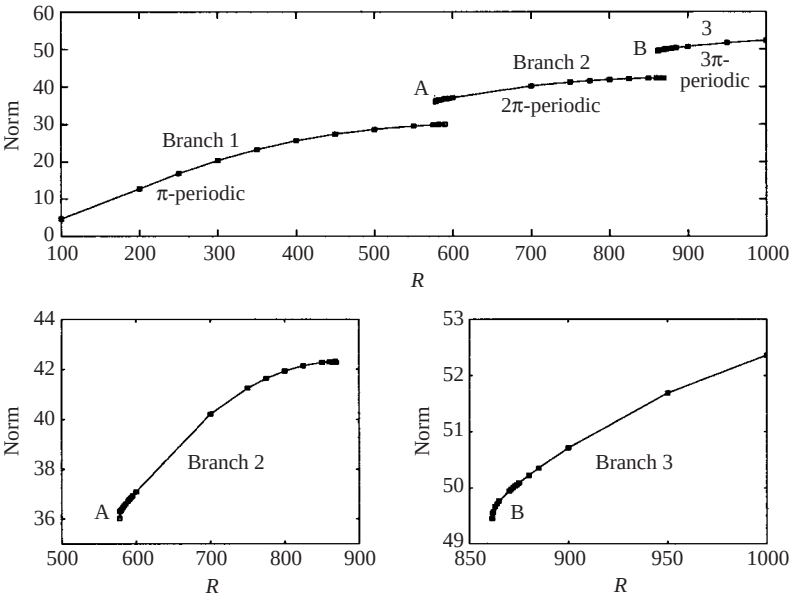

FIGURE 16. Bifurcation diagram $\Delta = 0.6$. Lower figures are enlargements of branches 2 and 3.

$R = 1200$, 1400, 1600, 1800 we find time intervals where the solution is 7π-, 8π-, 10π-, 12π-periodic respectively. As mentioned, no long-lived chaotic solutions have been found at this value of Δ. Owing to the prohibitive cost of the calculations (typically we used 1200 grid points and a timestep of size 10^{-4}) we did not go beyond $R = 2000$, but we expect the scenario presented above to persist.

For $\Delta = 0.45$, then, there is a competition between aperiodic attractors and time-periodic solutions of periods which become increasingly large with Reynolds number, but which are integer multiples of the driving period, π. A clarification of these attractors is possible at even larger values of Δ, of which 0.6 is a representative example. At such large amplitudes, aperiodic behaviour is not observed and the flow remains time-periodic, at least for all the Reynolds numbers studied. We discuss this flow in full because it is completely different from the Feigenbaum routes to chaos discovered for the channel problem at sufficiently large Δ – see HP.

In figure 16 we show a picture of the bifurcations for Reynolds numbers less than 1000. A norm, defined below, is plotted against Reynolds number in different solution regions. The norm is defined by

$$Norm = \frac{1}{T}\int_{t_0}^{t_0+T} (F(1/4, t))^2 \, \mathrm{d}t, \tag{4.1}$$

where T is the period of the solution (an integer multiple of π) and t_0 is an arbitrary reference value where the integration begins and does not affect the final outcome. The three distinct branches shown support π-, 2π- and 3π-periodic solutions as R increases. The branches are disjoint in the sense that there is not a smooth supercritical bifurcation that leads from one branch to the next. (Note that a smooth bifurcation can lead to period doubling, quadrupling etc., but it is not possible to go smoothly from a 2π- to a 3π-periodic solution, for example.) This picture persists at higher Reynolds numbers and we find solutions having periods which are sequentially larger

Window	Type of attractor	Scale factor λ
$0 < R \leqslant 590$	π-periodic	–
$578 \leqslant R \leqslant 869$	2π-periodic	–
$861.5 \leqslant R \leqslant 1075$	3π-periodic	–
$1100 \leqslant R \leqslant 1250$	4π-periodic	1.51 ($R = 1250$)
$1300 \leqslant R \leqslant 1450$	5π-periodic	1.43 ($R = 1425$)
$1453 \leqslant R \leqslant 1500$	6π-periodic	1.41 ($R = 1470$)
$R = 1700$	7π-periodic	1.35
$1800 \leqslant R \leqslant 1900$	8π-periodic	1.30 ($R = 1900$)
$R = 3000$	16π-periodic	1.18

TABLE 1. Overview of numerical results for $\Delta = 0.6$.

integer multiples of π. In the lower part of figure 16, we show the details of the branches 2 and 3 in the regions where they overlap with the branches 1 and 2 respectively. The stable branches computed are seen to terminate at limit points (labelled A and B respectively); for values of R above the given limit point, a stable and an unstable part of the same branch co-exist, with the unstable one not shown because our numerical methods are based on solving initial value problems and can only compute stable branches. From a practical point of view, it was found that in order to calculate the branches in the neighbourhoods of A and B as the Reynolds number decreases, a delicate continuation had to be used to avoid the solution jumping onto the more strongly attracting branch below (branch 1 for the limit point A and branch 2 for B). Briefly, this was done as follows: Given a periodic solution at a Reynolds number R_0, say, just above A or B, a solution on the same branch was calculated by using this as initial conditions and computing with a dynamic Reynolds number $R = R_0 - \overline{R}\tanh(\alpha t)$, where α is a measure of how slowly varying the tanh function is (typical values are in the range 0.05–0.2). For values of $\alpha t > 10$, the Reynolds number is practically equal to $R_0 - \overline{R}$ and was fixed to this value for the remainder of the calculation, which was continued to convergence. As the limit points are approached, the values of the decrements $\overline{R}$ had to be taken smaller and smaller, reaching values of 0.025 or less.

The different periodic attractors identified by our calculations are summarized in table 1. We expect the pattern to continue to higher Reynolds numbers. On each individual branch we have found that the solutions possess a self-similar structure, which is best described by considering an individual case, which we do next.

4.3. *The case* $\Delta = 0.6$, $R = 1700$

In considering this particular example we aim to highlight certain spatio-temporal self-similarity at different Reynolds numbers for $\Delta = 0.6$. To elucidate this, we begin by showing in figure 17 a plot of several time traces, sampled at different radial locations after transients have decayed, along with the wall function $H(t)$. The calculation was initiated with zero flow. The flow is 7π-periodic and the signal, taken from positions sufficiently far from the wall, consists of seven individual peaks per cycle a distance π apart. Note that the axial velocity is in phase with $H(t)$, while the radial velocity at $\eta = 1/4$ is out of phase. Such features are absent closer to the wall, for example for $u(3/4, t)$, where it is also observed that the radial velocity has switched sign and is now in phase with the wall oscillation. Further consideration of spatial features follows below.

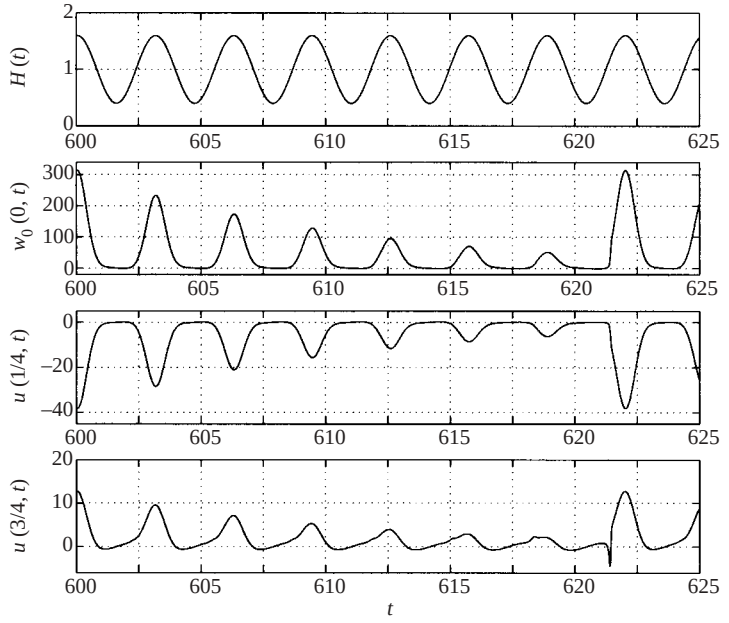

FIGURE 17. The time signals $H(t)$, downpipe velocity $w_0 = 2F_r(0, t)$, and radial velocities $u(1/4, t) = -F(1/4, t)$, $u(3/4, t)$ for $\Delta = 0.6$, $R = 1700$.

The individual pulses appear to be self-similar, and this can be confirmed by rescaling and overlaying successive peaks. Defining λ to be the ratio of successive maxima (starting from the largest one) of the signal $F(1/2, t)$, we find that the scale factor, λ, is the same across one period with errors of less than 1% entering for the last few peaks. This strongly suggests that peaks decay geometrically every π time units over the given period which is of length $n\pi$. These results are summarized in table 1. We remark that λ decreases slowly with Reynolds number.

Despite the relatively clear time signals seen above, we have determined numerically that over the 7π period, unsteady, nonlinear and viscous terms compete in a complicated manner. Over parts of the cycle, all three sets of terms have comparable magnitudes across the whole flow field. Thus viscous terms are active even up to the pipe centre line during some parts of the period. However, over the peaks, where both F and G become relatively large, the nonlinear terms alone dominate. At these times we find that the solution for $F(\eta, t)$ across the flow field resembles very closely a Bessel function of order one half. To explain this, we observe that with both R and F large the governing equations (2.4a, b) may be written, to a first approximation, as

$$-\widetilde{F}\widetilde{G}_\eta + \widetilde{F}_\eta\widetilde{G} + \frac{2\widetilde{F}\widetilde{G}}{\eta} = 0, \tag{4.2a}$$

$$\widetilde{F}_{\eta\eta} + \frac{1}{\eta}\widetilde{F}_\eta - \frac{1}{\eta^2}\widetilde{F} = -H^2\widetilde{G}, \tag{4.2b}$$

where $\widetilde{F}$, $\widetilde{G}$ are rescaled variables. The boundary conditions are $\widetilde{F}(0, t) = 0$, $\widetilde{G}(0, t) = 0$, and the inviscid no-penetration condition on the moving wall, $\widetilde{F}(1, t) = 0$. Equation (4.2a) may be integrated exactly and using this result to eliminate $\widetilde{G}$ from (4.2b)

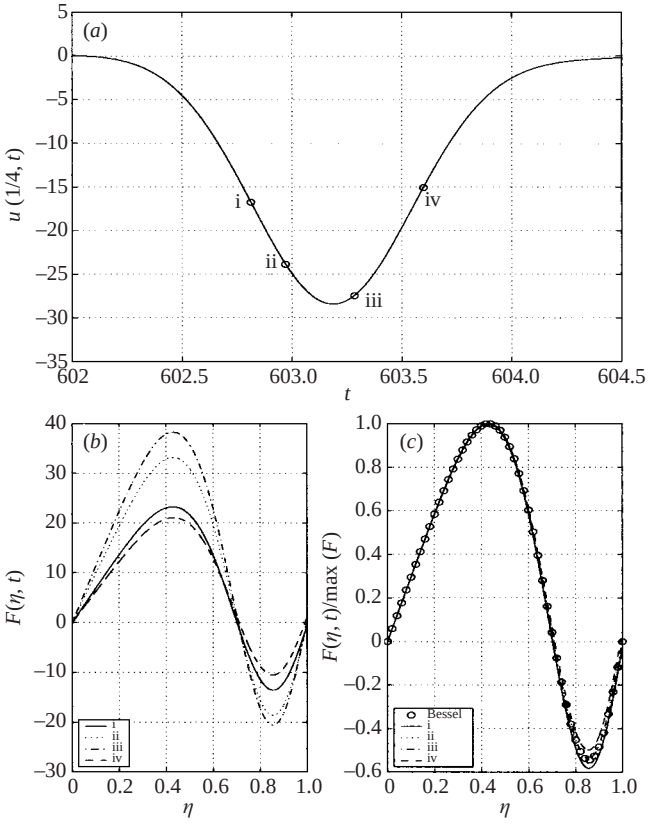

FIGURE 18. Comparison with the Bessel solution. (*a*) Part of the time trace $u(1/4, t)$ with sample points (i, ii, iii, iv) at which times the profiles $F = -u(\eta, t)$ are plotted in (*b*). In (*c*) the profiles are rescaled on their maximum values and plotted together with a normalized version of solution (4.3), which is shown as circles.

produces the exact solution

$$\widetilde{F} = A(t)\,\mathrm{J}_{1/2}(k\eta^2) = \left(\frac{2}{k\pi}\right)^{1/2} A(t)\,\frac{\sin k\eta^2}{\eta}, \tag{4.3}$$

where J is the Bessel function of the first kind, and $A(t)$ is an unknown function of time. The boundary condition at the wall then requires that $k = m\pi$, for some integer m. We make the choice $m = 2$ solely to agree with our numerical calculations. To validate this inviscid structure, we plot profiles of F across the pipe at various times over a particular peak. Figure 18(*a*) shows part of the second peak occurring in the $u(1/4, t)$ trace seen in figure 17. Profiles of F are plotted in 18(*b*) at times corresponding to the points indicated on the time signal. In 18(*c*) are shown the profiles at the four sample times and the Bessel solution (4.3), all normalized so that their maximum values are equal to one. The excellent agreement between the profiles is good evidence of the validity of (4.3) during this part of the cycle. In particular we note that the rescaled profile (iii), at which point F and G are nearly at their largest, is indistinguishable from the Bessel solution. This universality after normalization is possible due to the separable nature of the solution (4.3). It has been numerically confirmed that this inviscid structure also holds true over the other peaks in the cycle.

Referring to the typical situation of figure 18, as we move forwards in time from point (iv) the unsteady and viscous terms come into play, destroying this structure. This implies that, even though the Reynolds number is large, the full equations must be solved in order to connect one self-similar inviscid structure to the next. We attempted a large Reynolds number analysis that confines viscous effects to the boundary layer for all time. This analysis has not proven successful in describing the rich dynamics reported here.

5. The steady-streaming limit $\Delta \to 0$, $R \to \infty$

The numerical results of §4.1 suggest that the scaling $\Delta = O(R^{-1/2})$ is important as $\Delta \to 0$, since it marks the boundary between synchronicity with the wall forcing and the onset of quasi-periodic flow. In this section we establish the asymptotic structure associated with this scaling. We therefore start by assuming the large-R relationship

$$\Delta = dR^{-1/2},$$

for some unknown constant d. This limit has also been briefly discussed by Secomb (1978).

If we eliminate G from the governing equations (2.4), we obtain a single equation for F. This can be simplified somewhat by making the transformation $F = -\dot{H}\eta - 2H^5 f(\eta, t)/\eta$ and introducing the new variable $y = \eta^2$. In this way we derive the single governing equation

$$\tfrac{1}{4} f_{yyt} + H^4(f f_{yyy} - f_y f_{yy}) = \frac{1}{H^2 R}(y f_{yyyy} + 2 f_{yyy}), \tag{5.1}$$

which is strikingly similar to that obtained in the two-dimensional case (see HP). The boundary conditions are of course different. They are

$$f(0, t) = 0, \quad \lim_{y \to 0} \{ y^{1/2} f_{yy}(0, t) \} = 0, \tag{5.2a}$$

$$f(1, t) = 0, \quad f_y(1, t) = -\dot{H}/2H^5, \tag{5.2b}$$

and follow from (2.5). The proceeding asymptotic analysis runs along the same lines as that in HP. When R is large we infer the existence of a boundary layer of thickness $O(R^{-1/2})$ at the wall, in which the dominant balance is between the unsteady and viscous terms. We therefore introduce the wall variable $\zeta = R^{1/2}(1 - y)$. The form of the boundary conditions suggest that in the boundary layer the expansion

$$f = R^{-1} f_0(\zeta, t) + R^{-3/2} f_1(\zeta, t) + R^{-3/2} f_M(\zeta) + O(R^{-2}) \tag{5.3}$$

is appropriate. The solution details follow in the manner of HP; we therefore provide only the salient points. The zeroth-order equation is easily integrated to yield $f_0(\zeta, t)$. At next order all terms are averaged over time to produce an inhomogeneous equation for $f_M(\zeta)$ whose solution is again straightforward. Satisfying the boundary conditions, we find that this solution has the property,

$$f_M \sim -6d^2\zeta \quad \text{as} \quad \zeta \to \infty, \tag{5.4}$$

and that f_0 is of order unity as we leave the layer. In the core part of the flow, where $y = O(1)$, we make the expansion

$$f = R^{-1} f_C(y, t) + R^{-1} R_s \phi(y, \tau) + O\left(R^{-3/2}\right), \tag{5.5}$$

where, by introducing the new variable $\tau = (R_s/R)t$, we allow for slow variation of ϕ on an $O(R)$ timescale, which is consistent with the numerical results of §4.1 (see

particularly figure 14*b*). The steady-streaming Reynolds number R_s is defined below, where its significance will become apparent.

The leading-order solution $f_C(y,t)$ is time-periodic with zero mean. Of greater interest here, however, is the steady-streaming term $\phi(y)$. Substituting (5.5) into (5.1) and integrating over a single time period, we obtain

$$\tfrac{1}{4}\phi_{yy\tau} + (\phi\phi_{yyy} - \phi_y\phi_{yy}) = \frac{1}{R_s}(y\phi_{yyyy} + 2\phi_{yyy}). \tag{5.6}$$

Here we have introduced the steady-streaming Reynolds number $R_s = 6d^2$ (see Stuart 1966). The boundary conditions are

$$\phi(0) = 0, \quad \lim_{y\to 0} y^{1/2}\phi_{yy}(0) = 0, \tag{5.7a}$$

$$\phi(1) = 0, \quad \phi_y(1) = 1. \tag{5.7b}$$

Condition (5.7*b*) follows from matching with the wall layer via (5.4).

At this stage an analogy may be drawn with the flow in a pipe with an accelerating wall, which is also governed by the system (5.6), (5.7). The sign on the Neumann boundary condition at the wall determines the direction in which the wall is accelerating. For our case it is towards the origin. Brady & Acrivos (1981) studied both the two-dimensional and axisymmetric versions of this problem when the wall is accelerating away from the origin (in which case $\phi_y(1) = -1$). These authors investigated the existence of steady solutions over the full range of R_s and showed that multiple solutions exist at some parameter values. Intriguingly, for the axisymmetric problem, they noted that no steady solutions exist in the range $10.25 < R_s < 147$. Using the numerical method described in that paper, steady solutions to our system (5.6), (5.7) have been computed for up to $R_s \simeq 6000$ and they appear to be unique. However, to tie in with our earlier numerical results we are primarily interested in time-dependent solutions of the equations. These may be found by adapting the code for the full problem developed in §3, and marching forward in time at a fixed R_s until transients have decayed. In this way the steady solutions computed using Brady & Acrivos's method were recovered, and the Reynolds number was increased until a Hopf bifurcation invoked the existence of time-dependent solutions. The location of this bifurcation was pinpointed by a linear stability analysis about the steady base state. Thus, if at a fixed R_s the steady solution is $\phi_B(y)$, we write

$$\phi = \phi_B(y) + \mathrm{e}^{s\tau}\widetilde{\phi}(y),$$

where $\widetilde{\phi}$ is assumed small, and solve the resulting eigenvalue problem for s. This can be done by marching a linearized form of the previous code forward in time from any given initial conditions until s equilibrates, or by treating it as a generalized eigenvalue problem and solving for all s. The latter calculation produces the results shown in figure 19. The first eigenvalue to cross the real axis is complex and thus represents a Hopf bifurcation. This occurs at $R_s \simeq 592.27$. Comparison can now be made with the numerical results for the full problem in §4.1. Taking the fitted line of gradient -2.0 in figure 13(*b*) we use the intercept with the $\log R$-axis to predict $d \simeq 9.2$. The value of R_s for the Hopf bifurcation calculated above gives $d \simeq 9.9$. The agreement is relatively good.

Beyond the Hopf bifurcation the solutions are periodic, with period an increasing function of the Reynolds number R_s. For the channel problem, HP found that as the steady-streaming Reynolds number was increased a period doubling on the second frequency occurred, leading ultimately to chaos. The length ratios of the successive

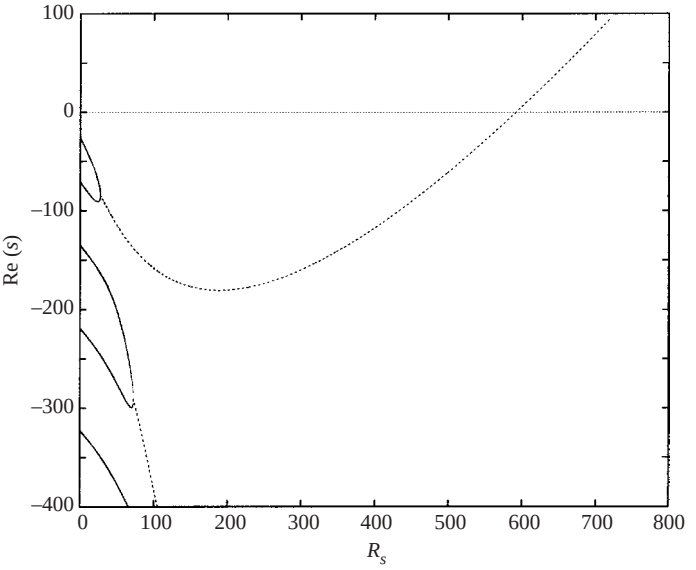

FIGURE 19. Real part of the calculated growth rates s versus R_s for the perturbed steady-streaming problem. A solid line means that s is real, while a broken line indicates a complex conjugate pair. The Hopf bifurcation occurs at $R_s \simeq 592.27$.

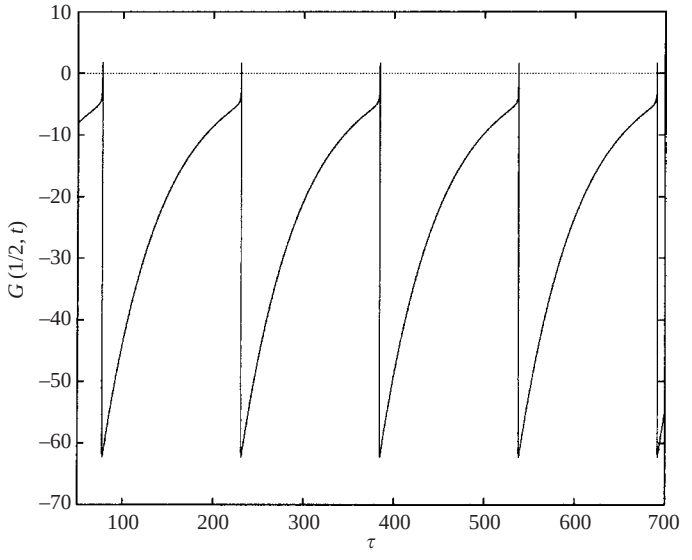

FIGURE 20. Time series $G(1/2, \tau)$ when $R_s = 5000$.

periodic subwindows agreed well with Feigenbaum's theoretical value (Feigenbaum 1979, 1980) for such a cascade in the case of discrete maps. However, for the axisymmetric problem, in stark contrast to the two-dimensional results, we have found no chaos at any values of R_s. As the steady-streaming Reynolds number is increased beyond the initial Hopf bifurcation, the flow remains periodic (with period depending on R_s) and apparently no chaotic regime is ever reached. We computed the flow for Reynolds numbers up to about 20 000 without encountering any further bifurcations. Figure 20, where $R_s = 5000$, shows how for larger Reynolds numbers

the time signal develops a periodic sequence of spikes, representing very short bursts of intense acceleration.

6. Concluding remarks

We have considered incompressible flow in a cylindrical pipe whose wall oscillates in a prescribed periodic manner. This problem represents the axisymmetric counterpart of the pulsating channel flow studied by Hall & Papageorgiou (1999). In both cases a stagnation-point structure is assumed. This simplifies the governing system to a partial differential equation involving time and one spatial coordinate. For the two-dimensional case, Hall & Papageorgiou uncovered a rich set of flow dynamics, including periodic, quasi-periodic and chaotic solutions. The same is true for the axisymmetric case studied here, although the new geometry introduces some notable differences. At fixed wall amplitude, as the Reynolds number is increased, the flow remains in synchrony with the wall movement until the Reynolds number passes through a critical value. At this point a Hopf bifurcation occurs, introducing a new frequency and leading to quasi-periodic flow. The location of this critical point and the dynamics occurring thereafter are dependent on the size of the wall amplitude. In general periodic, quasi-periodic and chaotic attractors may exist. We have studied the axisymmetric flow for small, moderate and larger values of the wall amplitude. Since our numerical method evolves the solution from an initial state (usually that of zero flow), it converges to the most stable solution for any fixed set of the parameter values. Thus, while several different competing attractors may exist at any one point in parameter space, our solution picks out only the most attracting one. However, particularly for the larger amplitude dynamics, we have been able to follow a specific solution branch by means of a continuation method.

For intermediate values of the wall amplitude, periodic attractors exist with periods distinct from that of the driving motion. However, when the Reynolds number is taken to be sufficiently large, our results suggest that the flow always descends into chaos. The situation is quite different when the amplitude is small. In this case, the quasiperiodic flow arising at the first bifurcation continues indefinitely, with no further periodic attractors being encountered, and more importantly without the appearance of chaos. For wall amplitudes as small as 0.075 we have taken the Reynolds number to be as large as 2×10^4, where the flow is still quasiperiodic. In the small-amplitude, large-Reynolds-number limit, an asymptotic analysis is possible. This leads to a steady-streaming system active over the majority of the flow field, whose own stability to time-dependent solutions may be examined. We found that a single Hopf-bifurcation induces a stable time-dependent solution of the steady-streaming equations, but, as the steady-streaming Reynolds number was increased, no period-doubling cascade to chaos was ever encountered. This is consistent with the persistence of quasi-periodic flow found in the full numerical simulations, but is in contrast to the two-dimensional case and seems to be a direct result of the axisymmetric geometry.

At the larger values of the wall amplitude, the situation is also noticeably different from the channel flow. In that case a Feigenbaum period-doubling cascade to chaos was identified, with a number of periodic attractors existing just beyond. For the axisymmetric problem, we have found no evidence of chaos at large amplitudes. Instead, a succession of periodic attractors were found, with periods equal to sequentially larger integer multiples of π. On any one of these $n\pi$-periodic branches

the solutions possess striking self-similar inviscid structures not identified in the two-dimensional case.

In none of the instances where it occurs have we been able to identify a period-doubling route to chaos; rather the transition appears to be abrupt, with no preceding cascade.

Finally, we make some comments on the physical significance of our work. Reintroducing physical units, we see that if B represents the dimensional amplitude of wall vibrations, then our analysis predicts the onset of quasi-periodic flow when

$$B = 9.9\left(\frac{\nu}{n}\right)^{1/2} + \cdots$$

for high-frequency (large n) oscillations. Here we have used the larger of the two figures quoted for d in §5, which comes from the asymptotic analysis. Taking water as an example fluid (so $\nu = 10^{-6}\,\mathrm{m^2\,s^{-1}}$), we see that for frequencies of 1000 Hz, 100 Hz and 10 Hz, wall amplitudes of only 0.18 mm, 0.56 mm and 1.77 mm respectively are required to produce quasi-periodic flow, although our work suggests that increasing the frequency will never result in chaos; larger wall amplitudes may move the flow into the chaotic regime.

Regarding the TMLR process mentioned in the introduction, the tunnels drilled into the heart muscle are of approximate diameter 0.5 μm and the wall oscillations are expected to be of typical frequency 1 Hz (Waters 2001). Blood has a kinematic viscosity of about $4 \times 10^{-6}\,\mathrm{m^2\,s^{-1}}$ at normal body temperature (37°C) (Pedley 1980). This flow has a Reynolds number of 1.6 which is well below the first Hopf bifurcation for any value of the wall amplitude. Waters uses a two-dimensional model and assumes that the blood flow remains synchronous with the wall motion. The present results show that this assumption would also be valid for an axisymmetric model.

For drop-on-demand ink jet printing, the wall amplitude is expected to be relatively large, the frequency very high and the pipe diameter very small. Taking $\overline{a} = 50\,\mu\mathrm{m}$, $\nu = 2.3 \times 10^{-6}\,\mathrm{m^2\,s^{-1}}$ as typical values for the mean pipe diameter and kinematic viscosity of printer's ink respectively, and assuming an operational frequency of 100 kHz, we find $R = 343$ as a characteristic Reynolds number. For sufficiently large amplitudes, this Reynolds number may well be large enough to produce the integer multiple of π-periodic regimes described in §4.3. While the piezo-driven pulsations in ink jet nozzles are in reality confined to a particular portion of the pipe, our similarity solution may still apply to some part of the flow field.

The work of D. T. P. was supported by the National Science Foundation (Grant DMS-007228).

REFERENCES

Bergé, P., Pomeau, Y. & Vidal, C. 1984 *Order Within Chaos – Towards a Deterministic Approach to Turbulence*. Wiley-Interscience.

Brady, J. F. & Acrivos, A. A. 1981 Steady flow in a channel or tube with an accelerating surface velocity. An exact solution to the Navier–Stokes equations with reverse flow. *J. Fluid Mech.* **112**, 127–150.

E, W. & Liu, J.-G. 1996 Vorticity boundary condition and related issues for finite difference schemes. *J. Comput. Phys.* **124**, 368–382.

Eckmann, J.-P. & Ruelle, D. 1985 Ergodic theory of chaos and strange attractors. *Rev. Mod. Phys.* **57**, No. 3, Part I, 617–656.

Feigenbaum, M. 1979 The onset of spectrum turbulence. *Phys. Lett.* B **74**, 375–378.

Feigenbaum, M. 1980 The transition to aperiodic behaviour in turbulent systems. *Commun. Math. Phys.* **77**, 65–86.

Hall, P. & Papageorgiou, D. T. 1999 The onset of chaos in a class of Navier–Stokes solutions. *J. Fluid Mech.* **393**, 59–87 (referred to herein as HP).

Horvath, K. A., Smith, W. J., Laurence, R. G., Schoen, F. K., Appleyard, R. F. & Cohn, L. H. 1995 Recovery and viability of an accute myocardial infarct after transmyocardial laser revascularization. *J. Am. Coll. Cardiol.* **25**(1), 258–263.

Ottino, J. M. 1989 *The Kinematics of Mixing: Stretching, Chaos and Transport*. Cambridge University Press.

Pedley, T. J. 1980 *The Fluid Mechanics of Large Blood Vessels*. Cambridge University Press.

Secomb, T. W. 1978 Flow in a channel with pulsating walls. *J. Fluid Mech.* **88**, 273–288.

Stuart, J. T. 1966 Double boundary layers in oscillatory viscous flows. *J. Fluid Mech.* **24**, 673–687.

Stuart, J. T., DiPrima, R. C., Eagles, P. M. & Davey, A. 1990 On the instability of the flow in a squeeze lubrication film. *Proc. R. Soc. Lond.* A **430**, 347–375.

Waters, S. L. 2001 Solute uptake through the walls of a pulsating channel *J. Fluid Mech.* **433**, 193–208.

Wolf, A., Swift, J. B., Swinney, H. L. & Vastano, J. A. 1985 Determining Lyapunov exponents from a time series. *Physica* **16D**, 285–317.